# Spinodal de-wetting of light liquids on graphene

Juan M. Vanegas,[1] David Peterson,[1] Taras I. Lakoba,[2] and Valeri N. Kotov[1]
[1] *Department of Physics, University of Vermont, Burlington, VT 05405*
[2] *Department of Mathematics and Statistics, University of Vermont, Burlington, VT 05405*

We demonstrate theoretically the possibility of spinodal de-wetting in heterostructures made of light–atom liquids (hydrogen, helium, and nitrogen) deposited on suspended graphene. Extending our theory of film growth on two-dimensional materials to include analysis of surface instabilities via the hydrodynamic Cahn–Hilliard-type equation, we characterize in detail the resulting spinodal de-wetting patterns. Both linear stability analysis and advanced computational treatment of the surface hydrodynamics show micron-sized (generally material dependent) patterns of "dry" regions. The physical reason for the development of such instabilities on graphene can be traced back to the inherently weak van der Waals interactions between atomically thin materials and atoms in the liquid. Similar phenomena occur in doped graphene and other two-dimensional materials, such as monolayer dichalcogenides. Thus two-dimensional materials represent a universal theoretical and technological platform for studies of spinodal de-wetting.

## I. INTRODUCTION

Van der Waals (VDW) forces control a wide variety of phenomena in nature as they represent interactions between neutral bodies. Such interactions depend on the polarizability of individual atoms and materials and therefore are sensitive to the geometry and screening of the Coulomb force which is ultimately responsible for the VDW interaction [1]. VDW interactions can play an especially important role near surfaces where they control wetting phenomena of liquids deposited on materials, contact angles, as well as pattern formation instabilities, such as spinodal de-wetting [2–5].

One of the greatest developments in condensed matter physics in the last two decades has been the discovery of novel two-dimensional (2D), atomically thin materials, such as graphene [6]. Numerous 2D materials structurally similar to graphene also exist, for example the large family of transition-metal dichalcogenides (e.g., $MoS_2$). These can form the building blocks of the so-called VDW heterostructures [7, 8]. There are several important features of 2D materials that make them uniquely attractive candidates for studies of liquid adsorption, wetting and related VDW-driven phenomena. (1) First, the polarization function of 2D materials can be calculated with great accuracy. This in turn leads to an excellent description of VDW forces. Moreover the polarization of graphene reflects its characteristic Dirac-like electronic dispersion which can be affected by external factors such as application of mechanical strain [9–11], change in the chemical potential (addition of carriers) [6, 12], change in the dielectric environment (i.e., presence of a dielectric substrate affecting screening), etc. This means that VDW-related properties can be in principle effectively manipulated. (2) Being purely 2D structures, materials like graphene can be engineered and arranged in various configurations. From the point of view of the present work, the possibility to have a "suspended" configuration, i.e., graphene without an underlying substrate, is the most important one. A liquid (of thickness $h$) formed on graphene in this configuration is shown in Fig. 1. This is one of several configurations suggested to be of particular interest for studies of wetting phenomena in Ref. [13]. It is important to note that graphene is impermeable even to small atoms [14, 15]. Because

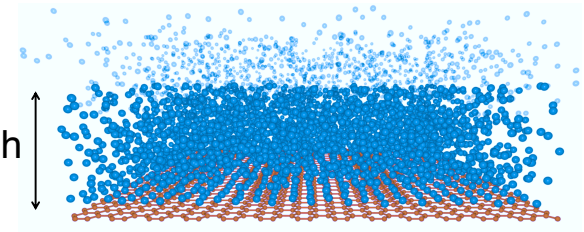


FIG. 1. Liquid film of thickness $h$ formed on suspended graphene.

an additional (bulk) substrate is not present in the case of suspended graphene, we will see that, as expected, graphene by itself exerts a relatively weak VDW force on the atoms of the film. This leads to the possibility of de-wetting at the liquid-vapor interface, and consequently a spinodal de-wetting pattern can form.

The purpose of the present work is to study in detail the conditions for spinodal de-wetting and the main characteristics of the surface spinodal patterns, for three light elements, He, $H_2$, and $N_2$, forming a liquid layer on top of suspended graphene. The phenomenon of spinodal de-wetting itself has a long history [16, 17] and has been theoretically predicted and detected in numerous situations involving polymers, liquid metals, etc. [3, 5, 18–28]. This type of de-wetting and the corresponding description bears much conceptual and technical similarity to spinodal decomposition which describes phase separation, commonly modeled via the Cahn–Hilliard equation (CHE) [29]. The main equation governing the fluctuations of the surface that describe spinodal decomposition (the analog of the CHE in this case) appear in the original literature [16]. We will use the formulation [20] which

adopts the notion of disjoining pressure $\Pi(h)$ – an effective repulsion between the substrate (graphene)–liquid and the liquid–vapor interface. A change in the sign of $\Pi(h)$ at a critical $h = h_c$ guarantees a minimum of $\Pi(h)$ at $h^* > h_c$, with a change in the sign of $d\Pi(h)/dh$ at $h^*$, signaling the onset of instability.

In order to calculate $\Pi(h)$, we rely on a previous work [13] where we present a detailed description of the gaphene–liquid–vapor configuration. In addition, the analysis of that work is also applicable to any atomically thin 2D material with liquid on top. It is based on the so-called Lifshitz theory (or Dzyaloshinskii–Lifshitz–Pitaevskii theory) [30, 31], which is the standard many-body approach for VDW forces in a three-layer (substrate–liquid–vapor) configuration with given dielectric functions. This approach provides a very reliable description, well verified by experiment for different substrates and liquids [1, 32]. The work [13] extends/modifies the original Lifshitz approach (designed for bulk materials) to the case of 2D substrates such as graphene. For the suspended configuration in Fig. 1 it was noted in [13] that $\Pi(h)$ goes through zero at $h_c$ and $d\Pi(h)/dh > 0$, $h > h^*$, for practically all 2D materials and atoms studied there. The values of $h_c$ and $h^*$ depend strongly on the type of liquid and 2D material substrate, but the existence of an instability appears to be generic to the suspended configuration. In the present work we study in detail the spinodal patterns that emerge.

The rest of the paper is organized as follows. In Section II we present results for the disjoining pressure for three types of light liquids on graphene. In Section III we analyze the surface hydrodynamics equation (CHE) and present results for the characteristic spinodal scales in the linear stability approximation as well as using finite element methods to numerically simulate the CHE. In Section IV we provide a detailed description of the spinodal de-wetting pattern formation and evolution. Section V contains our conclusions. In Appendix A we present details of the disjoining pressure calculation.

## II. DISJOINING PRESSURE FOR LIGHT LIQUIDS ON GRAPHENE

Our starting point is the analysis of Ref. [13], where the VDW interaction energy of the configuration in Fig. 1 was calculated. We consider three types of light atoms: He, $H_2$ and $N_2$. The energy is very sensitive to the atomic parameters, most notably the atomic polarizabilities, which are known quite accurately. The dynamical polarization of graphene is also well known and is an important ingredient of the calculation. For the purpose of studying the spinodal instability, it is convenient to introduce the disjoining pressure $\Pi(h)$, which is related to the derivative of the VDW energy as summarized in Appendix A.

The form of $\Pi(h)$ is an important ingredient for all subsequent calculations. Based on our previous results [13],

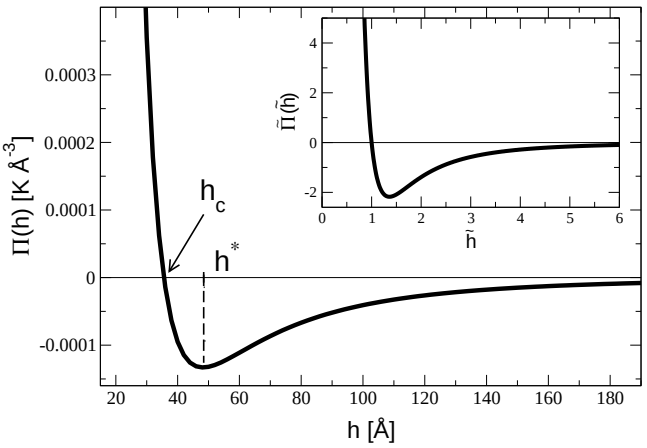


FIG. 2. Disjoining pressure $\Pi(h)$ for $N_2$. Inset: Dimensionless disjoining pressure as defined in the text, $\tilde{\Pi}(\tilde{h}) = \frac{\gamma^2}{\tilde{h}^3}\left(\frac{1-\tilde{h}}{\beta+\tilde{h}}\right)$, where $\tilde{h} = h/a$, and the notation $a \equiv h_c$ is defined in (2). The parameter $\beta = 0.37$, appropriate for $N_2$, and $\gamma = 5.13$ (see text).

which are summarized in Appendix A, the function $\Pi(h)$ can be parametrized with high accuracy in the following way:

$$\Pi(h) = \left\{-|\Pi_0| + \frac{\Pi_1}{h+L}\right\}\frac{1}{h^3} = \frac{|\Pi_0|}{h^3}\left(\frac{h_c - h}{h+L}\right). \quad (1)$$

The film thickness $h_c$ where $\Pi(h)$ changes sign, which from now we label as $a \equiv h_c$, depends on the parameters in the first part of the equation in the following way:

$$h_c = \frac{\Pi_1}{|\Pi_0|} - L \equiv a. \quad (2)$$

The crossover length $L$ is the characteristic length-scale which separates the $-1/h^3$ and $1/h^4$ behavior of $\Pi(h)$. As emphasized in [13] and Appendix A, the existence of this crossover in the range of distances relevant to wetting that we study here (up to several hundreds Å) is due to the fact that the dynamical polarization of graphene has a very strong momentum dependence, reflecting the motion of Dirac quasiparticles in the layer. Relativistic effects become important at much larger distances.

It is clear from Eq. (1) that $h = h_c(= a)$ is the point where $\Pi(h)$ changes sign. Our fits for the values of the relevant parameters for the three types of atoms, as explained in Appendix A, lead to the following results:

$$N_2: \quad |\Pi_0| = 72.8 \text{ K}, \ \Pi_1 = 3592 \text{ KÅ}, \ L = 13.3 \text{ Å}, \\ \Rightarrow a = 36 \text{ Å} \quad (3)$$

$$H_2: \quad |\Pi_0| = 14.5 \text{ K}, \ \Pi_1 = 1901 \text{ KÅ}, \ L = 18.0 \text{ Å}, \\ \Rightarrow a = 114 \text{ Å} \quad (4)$$

$$He: \quad |\Pi_0| = 2.09 \text{ K}, \ \Pi_1 = 676 \text{ KÅ}, \ L = 22.1 \text{ Å}, \\ \Rightarrow a = 301 \text{ Å} \quad (5)$$

A representative plot of $\Pi(h)$ for $N_2$ is shown in Fig. 2. The minimum of $\Pi(h)$ occurs at a distance which we label as:

$$h^* = (2a - L + \sqrt{(2a-L)^2 + 9La})/3. \quad (6)$$

It is worth noticing that the values of the critical distance $a$ (as well as $h^*$) are quite different for the three elements. Armed with the precise form of $\Pi(h)$, Eq. (1), we proceed to study spinodal de-wetting pattern formation.

## III. SURFACE HYDRODYNAMICS: CAHN-HILLIARD EQUATION AND SPINODAL DE-WETTING INSTABILITY

In this section we discuss the main equations of the theory and the linear stability analysis, appropriate for small initial perturbations of the surface. These are compared to numerical simulations based on the finite element method which provide a complete solution and describe the full evolution in space and time.

### A. Main Equations

The equation describing the evolution of $h$ has the form [5, 16, 20]:

$$\partial_t h = \boldsymbol{\nabla} \cdot \left\{ \frac{h^3}{3\eta} \boldsymbol{\nabla} \left( -\sigma \Delta h - \Pi(h) \right) \right\}. \quad (7)$$

This is the 2D analog of the CHE, which describes bulk phase separation. We use the standard notation:

$$h = h(x, y, t), \quad \boldsymbol{\nabla} = (\partial_x, \partial_y), \ \Delta = \boldsymbol{\nabla}^2 = \partial_x^2 + \partial_y^2. \quad (8)$$

Here $(x, y)$ is the in-plane coordinate, $\eta$ is the liquid viscosity and $\sigma$ is the surface tension (between the liquid and its vapor). Equation (7) has the standard form describing fluctuations of the surface [5, 16, 20]. The first term describes the resistance of the system to change of curvature (due to the Laplace pressure) and the second term is due to the disjoining pressure.

It is convenient to re-write the equation in dimensionless coordinates. First we observe that the following two dimensionless combinations can be constructed naturally

$$\alpha \equiv \frac{|\Pi_0|}{a^2 \sigma}, \quad \beta \equiv L/a \ . \quad (9)$$

Next, we choose to measure the height $h$ in units of the critical value $a$ and introduce new length and time scales $\xi, \tau$. The dimensionless height and space/time coordinates will be denoted by tilde:

$$\tilde{h} = h/a, \quad \tilde{x} = x/\xi, \quad \tilde{y} = y/\xi, \quad \tilde{t} = t/\tau. \quad (10)$$

By substituting this form into the main equation we find that we can choose:

$$\xi = \frac{a\gamma}{\sqrt{\alpha}}, \quad \tau = \frac{3\eta a}{\sigma} \frac{\gamma^4}{\alpha^2}, \quad (11)$$

where $\gamma$ is an arbitrary constant and will be commented on below. With these choices the original Eq. (7) becomes:

$$\partial_{\tilde{t}} \tilde{h} = \boldsymbol{\nabla} \cdot \left\{ \tilde{h}^3 \boldsymbol{\nabla} \left( -\Delta \tilde{h} - \tilde{\Pi}(\tilde{h}) \right) \right\}, \ \tilde{\Pi}(\tilde{h}) \equiv \frac{\gamma^2}{\tilde{h}^3} \left( \frac{1 - \tilde{h}}{\beta + \tilde{h}} \right). \quad (12)$$

For simplicity of notation from now on we use the same notation for gradients with respect to the dimensionless coordinates: $\boldsymbol{\nabla} = (\partial_{\tilde{x}}, \partial_{\tilde{y}})$, $\Delta = \boldsymbol{\nabla}^2 = \partial_{\tilde{x}}^2 + \partial_{\tilde{y}}^2$.

A plot of $\tilde{\Pi}(\tilde{h})$ is shown in Fig. 2. By construction, $\tilde{\Pi}(\tilde{h})$ changes sign at $\tilde{h} = 1$. We will summarize the values of the parameters and scales $\beta, \xi, \tau$ that appear in Eq. (12), for different liquids, in Section III B. In Section IV, we will use for convenience $\gamma = 5.13$ (for reasons described in Section III D). However, any other value can be used (notice that $\gamma$ appears both in $\tilde{\Pi}$ and the new scales $\xi, \tau$).

One can write Eq. (12) as a continuity equation

$$\partial_{\tilde{t}} \tilde{h} = \boldsymbol{\nabla} \cdot \tilde{\mathbf{J}} \quad (13)$$

where

$$\tilde{\mathbf{J}} = \tilde{h}^3 \boldsymbol{\nabla} \nu(\tilde{h}) \quad (14)$$

is the dimensionless particle flux vector field. Here we have defined for convenience the quantity $\nu(\tilde{h}) = -\Delta \tilde{h} - \tilde{\Pi}(\tilde{h})$, later used in our numerical simulations, Section III C. It follows from the form of Eq. (13) that the mass of the liquid over a given area of the substrate is conserved, provided appropriate boundary conditions are enforced. Indeed, integrating over a surface $\tilde{S}$ in the $\tilde{x}, \tilde{y}$ plane and applying the 2D version of the divergence theorem, we obtain $\partial_{\tilde{t}} \int \tilde{h} d\tilde{S} = \int \tilde{h}^3 (\boldsymbol{\nabla} \nu \cdot \hat{n}) dl$, where the integral is over the boundary curve $C$ and $\hat{n}$ is unit normal vector to the boundary. The boundary condition used in Section III C is

$$\boldsymbol{\nabla} \nu \cdot \hat{n} = 0 \ \text{ on } C, \quad (15)$$

implying the conservation of dimensionless "mass" $M = \int \tilde{h} d\tilde{S}$. (The mass with all units restored is $n_{\text{liquid}} \int h dS$, where $n_{\text{liquid}}$ is the liquid density.)

### B. Summary of Parameters for $N_2$, $H_2$, He

In the following sections, we characterize the short and long time scale behavior of the CHE through linear stability analysis and numerical simulations. Therefore, we summarize here the relevant scales and physical parameters for different liquids:

$$N_2 : \beta = 0.37, \ a = 36 \text{ Å}, \ h^* = 49 \text{ Å}, \\ \xi = 409\gamma \text{ Å}, \ \tau = 4\gamma^4 \ \mu\text{s} \quad (16)$$

$$H_2 : \beta = 0.16, \ a = 114 \text{ Å}, \ h^* = 153 \text{ Å}, \\ \xi = 4116\gamma \text{ Å}, \ \tau = 392\gamma^4 \ \mu\text{s} \quad (17)$$

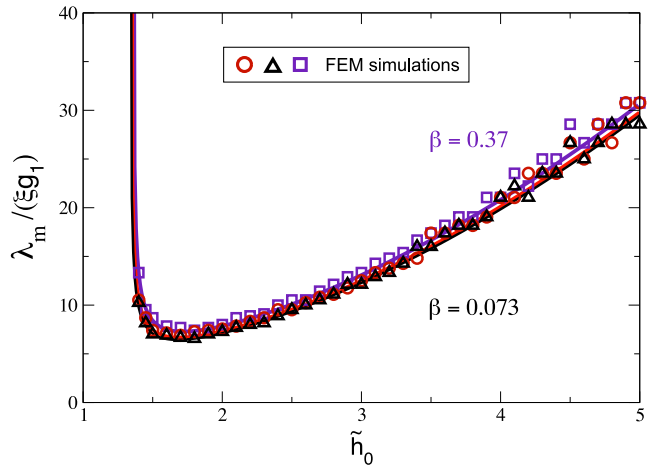


FIG. 3. The dimensionless spinodal wavelength $\tilde{\lambda}_m = \lambda_m/\xi$, normalized to $g_1$ (see (22a)) versus the dimensionless uniform film height $\tilde{h}_0 = h_0/a$. For $\beta = 0.37$ (blue), the value for $N_2$, the onset of instability is at $\tilde{h}^* = 1.359$. For $\beta = 0.16$ (red), the value for $H_2$, the onset of instability is at $\tilde{h}^* = 1.346$. For $\beta = 0.073$ (black), the value for He, the onset of instability is at $\tilde{h}^* = 1.339$. Symbols correspond to values obtained from FEM simulations.

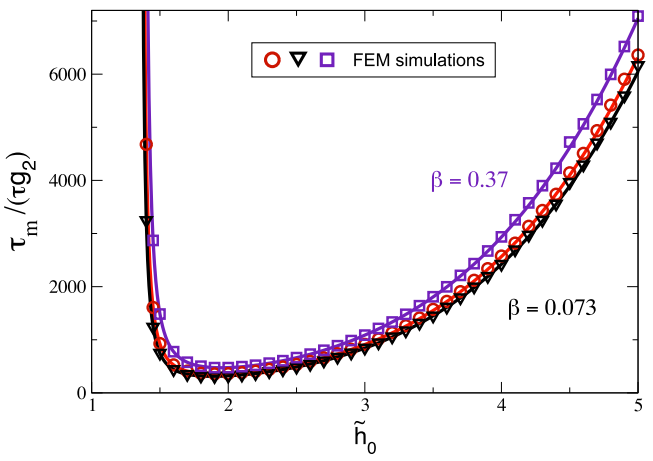


FIG. 4. The dimensionless time constant characterizing spinodal growth, $\tilde{\tau}_m = \tau_m/\tau$ normalized to $g_2$ (see (22a)), versus the dimensionless uniform film height $\tilde{h}_0 = h_0/a$. The dependence on $\beta$ is more pronounced compared to the wavelength $\lambda_m$. Symbols correspond to values obtained from FEM simulations.

$$\text{He} : \beta = 0.073,\ a = 301\ \text{Å},\ h^* = 403\ \text{Å},$$
$$\xi = 27197\gamma\ \text{Å},\ \tau = 75.5\gamma^4\ \text{ms} \tag{18}$$

The values of $\beta, a, h^*$ are based on (3),(4),(5),(6),(9), while $\xi, \tau$ follow from (11) where the following values of the surface tension and viscosity are taken from standard tables and literature found in [33]. For $N_2$ at temperature 70 K, $\sigma = 10$ mN/m, $\eta = 220$ $\mu$Pa·s; for $H_2$ at temperature 20 K, $\sigma = 2$ mN/m, $\eta = 13.5$ $\mu$Pa·s; for He at temperature 2.5 K, $\sigma = 0.26$ mN/m, $\eta = 3.26$ $\mu$Pa·s. The temperatures are chosen so that a liquid phase exists.

We observe that the parameter $\beta$, which appears in Eq. (12), has quite different values depending on the type of liquid, although we find that the solution depends on $\beta$ relatively weakly. More importantly, the relevant length and time scales can differ by orders of magnitude.

### C. Finite Element Simulations

Numerical simulations of Eq. (12) were performed in Python with the FEniCS automated finite element method (FEM) package [34–36]. A standard Lagrange finite-element basis was used to solve the the partial differential equation (first-order in time and fourth-order in space) by casting the weak form of the CHE as two coupled equations (Eqs. (13) and (14)) that are solved variationally [35]. Time integration was performed using the standard finite difference Crank–Nicolson method [37]. Sufficiently small time steps were chosen in order to facilitate convergence of the FEM solvers depending on the parameters for each species (see Table I) and film thickness values. Numerical accuracy was monitored by checking conservation of total mass at each time step ($\frac{dM}{M_{\text{total}}} < 10^{-14}$).

The starting condition for all simulations corresponded to the spatially uniform film of thickness ($\tilde{h}_0$) with very small random fluctuations ($< \tilde{h}_0 \times 10^{-5}$). Neumann boundary conditions were applied at the edges of the simulation box (Eq. (15)). Analysis of the FEM simulations was performed with the NumPy and SciPy libraries [38, 39].

### D. Linear Stability Analysis

It is known that the spinodal decomposition (instability) regime starts at the value of $h$ corresponding to the minimum of $\tilde{\Pi}(\tilde{h})$ [20]. In our dimensionless notation, $\tilde{h}^* = h^*/a$, the minimum is located at

$$\tilde{h}^* = [(2-\beta) + \sqrt{(\beta-2)^2 + 9\beta}]/3. \tag{19}$$

Thus, the instability regime occurs for $\tilde{h} > \tilde{h}^*$, where $\tilde{\Pi}(\tilde{h})$ is negative and its derivative is positive. Let us see in more detail how the instability develops within the framework of linear stability analysis [16, 17].

We apply a small-amplitude perturbation ($\varepsilon$) at a given wavenumber $\tilde{k}$ and imaginary frequency $\tilde{\omega}$ (both dimensionless), i.e., $\tilde{h}(\tilde{x}, \tilde{y}, \tilde{t}) = \tilde{h}_0(1 + \varepsilon\ e^{i\tilde{\boldsymbol{k}}\cdot\tilde{\boldsymbol{r}}} e^{-\tilde{\omega}\tilde{t}})$, where $\tilde{h}_0$ is the initial uniform film height. By expanding to first order we obtain

$$\tilde{\omega}(\tilde{k}) = \tilde{h}_0^3 \tilde{k}^2 \left(\tilde{k}^2 - \tilde{k}_c^2\right), \tag{20}$$

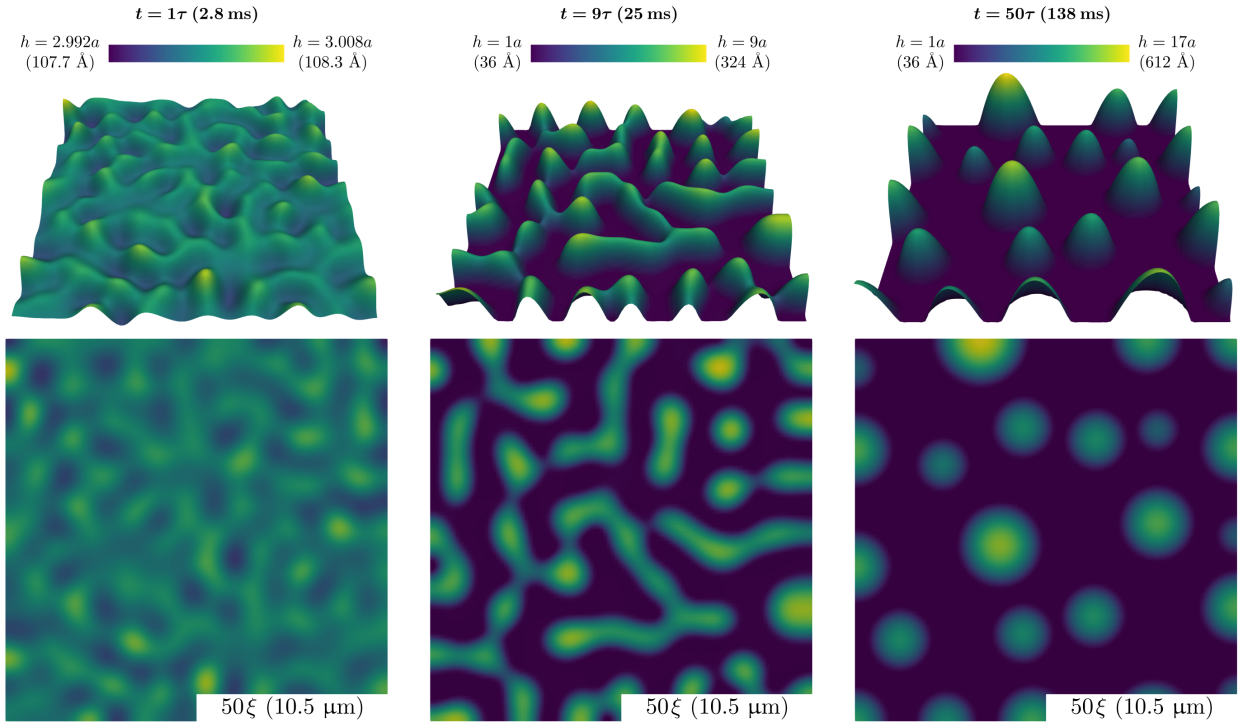


FIG. 5. Spinodal de-wetting time evolution observed in FEM simulation of $N_2$ on graphene for a liquid of initially uniform height $\tilde{h}_0 = 3.0$ (above $\tilde{h}^* = 1.36$). During the initial stages of the simulation, the initial random fluctuations ($< \tilde{h}_0 \times 10^{-5}$) lead to gradually increasing variations in the liquid height (left panel). These eventually form a well-defined spinodal de-wetting pattern (middle panel) where interconnected regions with excess liquid, $\tilde{h}(x,y) > \tilde{h}^*$, (light green/yellow colors) are surrounded by nearly flat regions with liquid height satisfying: $1 \lesssim \tilde{h}(x,y) < \tilde{h}^*$ (dark blue color). Note that the fact that $\tilde{h}(x,y) < \tilde{h}^*$ in the background regions is consistent with that reported in the literature; see, e.g., [23]. At long times, the regions of excess liquid continuously merge into larger "lumps".

where the critical wavenumber, $\tilde{k}_c$, is defined by:

$$\tilde{k}_c^2 = \frac{\gamma^2}{\tilde{h}_0^4}\left(\frac{\tilde{h}_0 - 1}{\tilde{h}_0 + \beta}\right)\left[3 - \frac{\tilde{h}_0(1+\beta)}{(\tilde{h}_0 - 1)(\tilde{h}_0 + \beta)}\right] = \frac{d\tilde{\Pi}(\tilde{h}_0)}{d\tilde{h}_0}. \tag{21}$$

Note that $\tilde{k}_c^2 > 0$ for $\tilde{h}_0 > \tilde{h}^*$.

When the quantity $\tilde{\omega}$ is negative, the solution is unstable. This happens for wavenumbers where $\tilde{k} < \tilde{k}_c$. The fastest growing mode is the one that has the largest $(-\tilde{\omega})$, which corresponds to the wavenumber $\tilde{k}_m = \tilde{k}_c/\sqrt{2}$. This maximum instability growth rate is $|\omega(\tilde{k}_m)| = \tilde{h}_0^3 \tilde{k}_m^4$, which leads to the time constant $\tilde{\tau}_m = (\tilde{h}_0^3 \tilde{k}_m^4)^{-1}$, meaning that the perturbation grows as $\sim e^{\tilde{t}/\tilde{\tau}_m}$. The spinodal wavelength (corresponding to the fastest growing mode) is $\tilde{\lambda}_m = 2\pi/\tilde{k}_m = 2\pi\sqrt{2}/\tilde{k}_c$.

According to (20), an unstable mode exists as long as $\tilde{k}_c^2 > 0$. From (21), one can show that this occurs for $\tilde{h}_0 > \tilde{h}^*$, where $\tilde{h}^*$ is defined in (19). Thus, films thicker than $\tilde{h}^*$ are unstable. For values of $\tilde{h}_0$ that significantly exceed $\tilde{h}^*$, one extracts the asymptotic behavior

$$\tilde{\lambda}_m \sim g_1\ \tilde{h}_0^2, \quad \tilde{\tau}_m \sim g_2\ \tilde{h}_0^5, \quad \text{for} \quad \tilde{h}_0 \gg 1, \tag{22a}$$

where

$$g_1 = \frac{2\pi\sqrt{2}}{\gamma\sqrt{3}}, \qquad g_2 = \frac{4}{9\gamma^4}. \tag{22b}$$

The choice $\gamma = 5.13$ results in $g_1 = 1$, which leads to a convenient form of the asymptotic dependence of the most unstable wavelength on the film height (in non-dimensional units). This is a convenient choice for the numerical simulations, but any other choice of $\gamma$ is also acceptable.

Plots of the spinodal wavelength (Fig. 3) and the spinodal growth time constant (Fig. 4) show divergence at the instability threshold and then increase as power laws for larger film heights. At the onset of instability, i.e., for $\tilde{h} \to \tilde{h}^* + 0$, the critical wavenumber is $\tilde{k}_c \sim (\tilde{h} - \tilde{h}^*)^{1/2}$, and therefore the spinodal wavelength, $\tilde{\lambda}_m \sim (\tilde{h} - \tilde{h}^*)^{-1/2}$, grows slowly (Fig. 3). On the other hand, the time scale of the instability, $\tilde{\tau}_m \sim (\tilde{h} - \tilde{h}^*)^{-2}$, diverges much stronger than the wavelength (Fig. 4). In Fig. 3 and Fig. 4 we also include values $\tilde{\lambda}_m$ and $\tilde{\tau}_m$ obtained from numerical simulations (see Section III C) by calculating a radially averaged 2D Fourier transform of $\tilde{h}(x,y)$ at each time step and identifying the fastest growing modes. We find excellent agreement between the re-

sults from linear stability analysis and numerical simulations across all values of the initial heights tested. The dependence on the parameter $\beta$, which varies with the type of liquid, is relatively weak, practically non-existent for $\lambda_m$ and somewhat more pronounced for $\tau_m$.

| Atom | $a$ | $\xi$ | $\tau$ | $\beta$ |
|---|---|---|---|---|
| $N_2$ | 36 Å | 209.8 nm | 2.77 ms | 0.37 |
| $H_2$ | 114 Å | 2.11 $\mu$m | 0.271 s | 0.16 |
| He | 301 Å | 13.9 $\mu$m | 52.3 s | 0.073 |

TABLE I. Time and length scales for different elements, computed from Eqs. (16)–(18) for $\gamma = 5.13$. Here $a$ represents the scale of the height $h$, and $\xi$ is the scale in the planar ($x$ and $y$) direction as introduced in Eq. (10), and $\tau$ is the time scale. The quantity $\beta$ is defined in (9).

## IV. TIME EVOLUTION OF SPINODAL DE-WETTING PATTERNS

The spinodal de-wetting patterns for $N_2$ (taken as an example) with $\tilde{h}_0 = 3$ obtained from numerical simulations are presented in Fig. 5 for three different times (corresponding to the free energy evolution in Fig. 6). These show the characteristic spinodal surface patterns as time increases, culminating in large height fluctuations at late times. For $N_2$ (Fig. 5), the observed distance between features at the initial/intermediate stages is $\sim 1$ $\mu$m in agreement with the spinodal wavelength values shown in Fig. 3 (in units of the length scale $\xi \approx 0.2$ $\mu$m, see Table I).

The observed time evolution of the liquid film can be

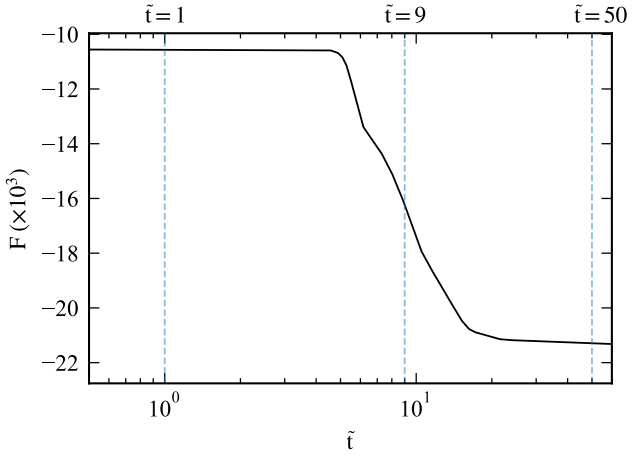


FIG. 6. Evolution of the free energy Eq. (23) with time for the $N_2$ film, obtained by FEM. Total value of the free energy depends on the area of the system ($A = 100\xi \times 100\xi$)

further characterized by considering the free energy:

$$F = \iint \left\{ \frac{1}{2} |\boldsymbol{\nabla} \tilde{h}|^2 + U(\tilde{h}) \right\} d\tilde{x} d\tilde{y}, \tag{23}$$

where the potential energy $U(\tilde{h})$ is defined as $\partial U / \partial \tilde{h} = -\tilde{\Pi}(\tilde{h})$,

$$U(\tilde{h}) = \frac{\gamma^2}{2\beta} \frac{1}{\tilde{h}^2} - \frac{\gamma^2(1+\beta)}{\beta^2} \frac{1}{\tilde{h}} + \frac{\gamma^2(1+\beta)}{\beta^3} \ln\left(1 + \frac{\beta}{\tilde{h}}\right). \tag{24}$$

The free energy in Eq. (23) decreases with time and is constant only on stable stationary solutions if/when they exist: $\frac{dF}{dt} \leq 0$ [20]. Values of the free energy for the $N_2$ numerical simulation are shown in Fig. 6. During the initial time evolution, $\tilde{t} < 5$, the small scale height fluctuations in the fluid are reflected in the approximately constant energy. At intermediate times, $5 < \tilde{t} < 20$, the energy rapidly changes as the spinodal fluctuations grow macroscopically and well-defined ridges of material accumulate above a nearly uniform film surface of thickness $\tilde{h} \gtrsim 1$ (see caption for Fig. 5). At larger time scales, $\tilde{t} > 20$, the energy enters a slowly changing regime as the ridges merge into "lumps" that accumulate the excess liquid. Based on this, the expected configuration of

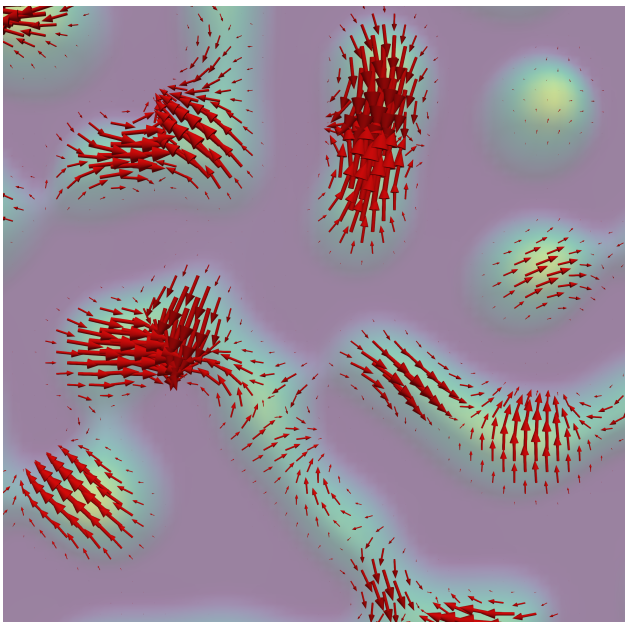

FIG. 7. Close-up of the flux vector field ($\tilde{\mathbf{J}}$, red arrows) for the $N_2$ FEM simulation shown in Fig. 5 (center panel). Arrow sizes are scaled by the magnitude of the flux vector at a particular $x - y$ location. Note how the flux vector field depicts different types of motions within the fluid including the translational motion of large features as well as the merging of neighboring ones (regions with high density of arrows). Height data shown in the background where purple/dark colors correspond to values of $\tilde{h} \approx 1$ and yellow/light green colors to $\tilde{h} \leq 9$.

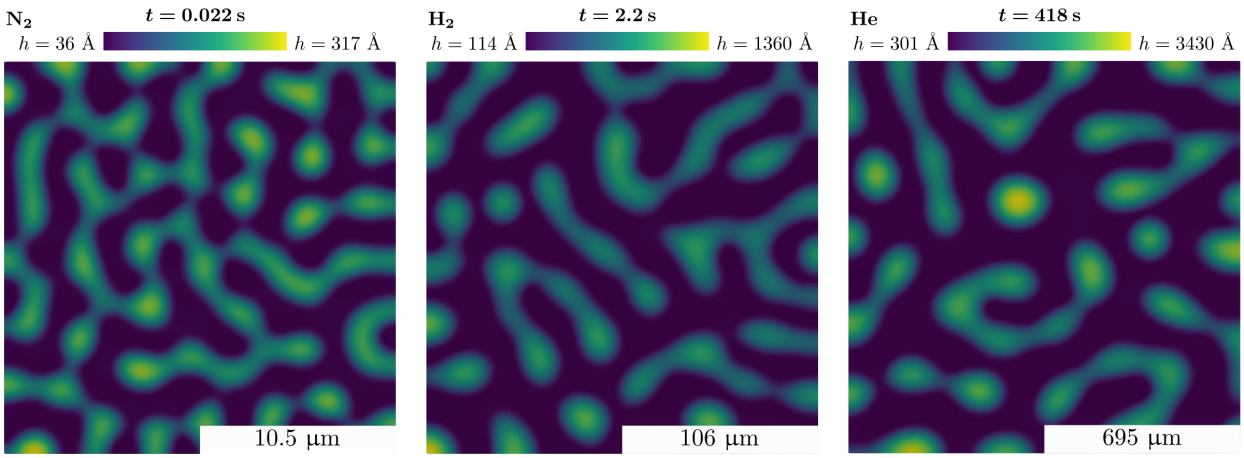


FIG. 8. Comparison of spinodal de-wetting patterns observed in FEM simulations of liquids on graphene for $N_2$ (left panel), $H_2$ (center panel), and He (right panel). For all three cases shown, the dimensionless parameters are the same ($\tilde{h}_0 = 3.0$, $t = 8\tau$, and $50\xi$ simulation size) except for $\beta$ (see Table I). While the patterns are qualitatively similar regardless of the liquid, the length and time scales are vastly different as discussed in the main text.

the liquid at an infinitely long time would show a single large-scale feature surrounded by a flat surface.

The redistribution of mass in the process of de-wetting can be more clearly observed with the help of the flux vector, $\tilde{\mathbf{J}}$, as shown in Fig. 7. While the total mass is conserved, as discussed previously, there is significant flow toward regions of larger height, relative to the uniform value.

Beyond $N_2$, the time and length scales for the three elements are quite different (Table I). Namely, the time scale is the shortest for $N_2$ and longest for He; this results in the evolution of He being much slower than that of the other two liquids in physical units. For example, for the nondimensional height $\tilde{h}_0 = 3$, the spinodal growth time scale for He is $\tau_m \sim 10$ s, while this time scale for $H_2$ and $N_2$ is $\sim 10^{-1}$ s, $10^{-3}$ s, respectively. Moreover, as shown in Fig. 8, the same *dimensionless* simulation time results in patterns corresponding to much later stages of evolution for He than for $H_2$ and $N_2$. Finally, for the same $\tilde{h}_0 = 3$, the characteristic spinodal wavelength for $N_2$ is $\lambda_m \sim 1$ $\mu$m, while for $H_2$ we have $\lambda_m \sim 10$ $\mu$m, and for He, $\lambda_m \sim 100$ $\mu$m.

## V. CONCLUSIONS

This work is devoted to prediction of surface de-wetting patterns for liquids on graphene. We emphasize that the first important step in the problem is the knowledge of the disjoining pressure $\Pi(h)$. This function can be determined very accurately for various elements on graphene since the atomic parameters and graphene's polarization can be calculated with great accuracy. In fact the general shape shown in Fig. 2 is quite universal and representative of numerous two-dimensional materials such as members of the dichalcogenides family ($MoSe_2$, $MoS_2$, $WSe_2$, $WS_2$). For all of these, the film thickness $h^*$ at which spinodal de-wetting starts (for He liquid) is between 100 Å and 300 Å [13]. Applying additional perturbations on graphene itself, such as electronic (or hole) doping via external voltage, also affects $h^*$, generally increasing it [13]. Therefore spinodal patterns are possible for liquids on all of those materials as well, the main difference being in the various characteristic length and time-scales which are very material specific. We also point out that the most important physical assumption in our analysis leading to Fig. 2 and everything that follows is that graphene (or any of the other 2D materials) are in the suspended configuration, since only in this case a finite $h^*$ is predicted, whereas the presence of an additional (bulk) substrate creates too much VDW attraction and sends $h^*$ to infinity. Of course the possibility of suspended configurations is one of the most exciting features of 2D materials.

The spinodal de-wetting patterns we predict (Fig. 5) for various liquids on graphene are quite universal in shape and time evolution when written in dimensionless form. The main difference is in the time and length-scales for different elements (Table I and Figures 3, 4). The spinodal wavelengths are generally quite long compared to the critical film thickness for spinodal onset (which is up to several hundred Å), and range between 1 $\mu$m and 100 $\mu$m depending on the liquid. On a technical level, our linear stability analysis and the full numerical analysis of the CHE are in excellent agreement (for weak initial perturbations and initial stages of pattern evolution). The full numerical implementation of course also provides detailed spinodal patterns and evolution of mass flow at long times and quite far from the instability threshold.

We hope this work stimulates further theoretical and experimental research related to the physics of spinodal de-wetting on 2D atomically thin crystals, especially

since this phenomenon appears to be a universal feature for this class of materials. We emphasize again the most important advantages of 2D materials, such as graphene:

– The spinodal de-wetting instability is a generic phenomenon in such materials and occurs spontaneously at the instability onset $h^*$ due to the fact that 2D structures are weak adsorbers, i.e., their VDW potential is not strong enough to maintain a film with uniform thickness in excess of $h > h^*$.
– Given that 2D material parameters are known with great accuracy, the spinodal de-wetting onset $h^*$ and the evolution of the spinodal de-wetting patterns can be reliably predicted for liquids with well-established polarization characteristics.
– Because graphene and 2D materials can be also manipulated via external factors such as carrier doping, strain, etc., this can be used as a guiding principle for creation and control of de-wetting patterns. For example a range of values $h^*$ was found in [13] for graphene and other 2D materials, such as monolayer dichalcogenides, which could lead to applications in micro-pattern design [24].

## ACKNOWLEDGMENTS

We are grateful to Adrian Del Maestro and Peter Taborek for numerous stimulating discussions related to the physics of wetting and wetting instabilities. J.M.V., T.I.L. and V.N.K. gratefully acknowledge financial support from NASA Grant No. 80NSSC19M0143.

## Appendix A: Details of Disjoining Pressure Calculations for Light Atoms on Graphene

Here we summarize the results of calculations related to the determination of the disjoinging pressure $\Pi(h)$, Eq. (1), which is used to extract the relevant parameters for different atoms, Eqs. (3),(4),(5). The form of Eq. (1) follows from microscopic Lifshitz theory, when applied to 2D materials, which describes VDW interactions in anisotropic (layered) situations such as liquids on solid substrates [1, 30, 31]. The standard calculations and typical applications assume a bulk (usually dielectric) substrate with a liquid formed on top, in equilibrium with its vapor. In [13] one of us and collaborators extended the standard theory to several physical situations involving 2D materials, and in particular to the case when a 2D semimetal, such a graphene, is used as a substrate instead of a bulk material (as shown in Fig. 1). We refer the reader to [13] for details of calculations. The ground state energy of this system can be written as (we set $\hbar = 1$):

$$U_{\rm vdW}(h) = \frac{1}{(2\pi)^3}\int d^2\mathbf{q}\int_0^\infty d\omega(\mathcal{U}_d(q,i\omega)+\mathcal{U}_g(q,i\omega)), \tag{A1}$$

where $\mathcal{U}_d(q,i\omega)$ describes the liquid with dielectric function $\varepsilon(i\omega)$ and thickness $h$, without a substrate and with liquid vapor on top (taken as vacuum, dielectric constant equal to one),

$$\mathcal{U}_d(q,i\omega) = \frac{(\varepsilon(i\omega)-1)(1-\varepsilon(i\omega))}{(\varepsilon(i\omega)+1)(1+\varepsilon(i\omega))}e^{-2qh}, \tag{A2}$$

and $\mathcal{U}_g(q,i\omega)$ is the graphene substrate–liquid interaction part:

$$\mathcal{U}_g(q,i\omega) = \frac{\left(\frac{-4\pi e^2\chi(q,i\omega)}{q(\varepsilon(i\omega)+1)}\right)\left(\frac{\varepsilon(i\omega)-1}{\varepsilon(i\omega)+1}\right)\left(\frac{2\varepsilon(i\omega)}{\varepsilon(i\omega)+1}\right)}{1-\frac{4\pi e^2\chi(q,i\omega)}{q(\varepsilon(i\omega)+1)}}e^{-2qh}. \tag{A3}$$

Equations (A2) and (A3) follow from more general expressions (describing different geometries) derived in [13]. Here $q = |\mathbf{q}|$ is the magnitude of the in-plane momentum and $\chi(q,i\omega)$ is graphene's polarization function which is known to be [12]:

$$\chi(q,i\omega) = -\frac{1}{4}\frac{q^2}{\sqrt{v^2q^2+\omega^2}}, \tag{A4}$$

where $v = 6.6\,\text{eV Å}$ is the velocity of the Dirac quasiparticles. We have modified somewhat the notations used in [13] in order to achieve consistency with the symbols across the present paper.

It should be emphasized that Eq. (A1) describes any 2D material (not only graphene), with a dynamical polarization $\chi(q,i\omega)$, in the suspended configuration. This allows one to compute the spinodal instability threshold $h^*$ and indeed the function $\Pi(h)$ with high accuracy. We also note that the energy in Eq. (A1) is written at zero temperature since finite-temperature effects in the VDW energy expression are negligibly small in the range of distances studied (as shown in Ref. [13](Supplementary Material)). Of course the various atom-related characteristics have to be used in the temperature regime where the liquid phase is stable, as in Section III B.

Several additional comments are in order. First, the fact that $U_{\rm vdW}(h)$ involves integration over the imaginary frequency axis is a common mathematical feature when writing the ground state energy of the system [1, 30, 31]. Second, notice that $\mathcal{U}_d(q,i\omega) < 0$, while $\mathcal{U}_g(q,i\omega) > 0$ (since we always have $\varepsilon > 1$ , which reflects screening). This will be important in what follows. Third, the terms $\mathcal{U}_d$ and $\mathcal{U}_g$ depend on $h$ only through the exponential factor. The nontrivial dependence of $U_{\rm vdW}(h)$ on $h$ arises after integration over the momentum $\mathbf{q}$. Notice also that graphene's polarization $\chi(q,i\omega)$ has a pronounced momentum dependence which reflects the motion of graphene's quasiparticles.

For completeness we also summarize the dielectric functions of the three liquids used in this work, as described in [13], which cites additional literature. For Helium the dynamical dielectric constant is

$$\varepsilon(i\omega) = 1+4\pi n_{\rm He}\alpha(i\omega), \quad \alpha(i\omega) = \frac{\alpha_{\rm He}}{1+(\omega/\omega_{\rm He})^2}, \tag{A5}$$

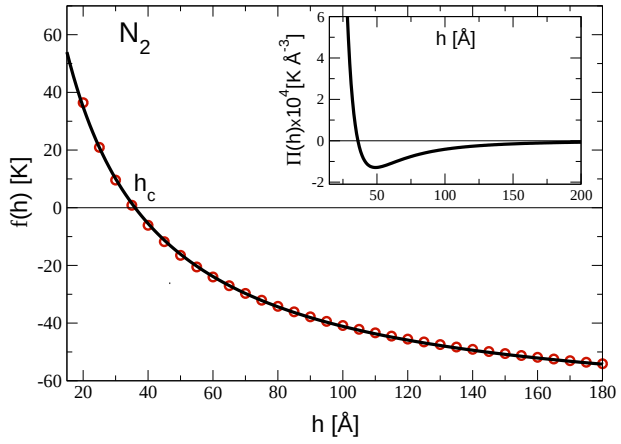


FIG. 9. The function $f(h)$, defined so that the disjoining pressure has the form $\Pi(h) = f(h)/h^3$. For $N_2$, $f(h)$ is calculated by evaluating the microscopic expressions Eqs. (A1),(A7), and is shown as a solid line in the main panel. The red circles represent a fit to the form $f(h) = -|\Pi_0| + \frac{\Pi_1}{h+L}$ (as in Eq. (1)), with $|\Pi_0| = 72.8$ K, $\Pi_1 = 3592$ KÅ, $L = 13.3$ Å. These are the values used in the main text, Eq. (3). Inset: The full function $\Pi(h) = f(h)/h^3$.

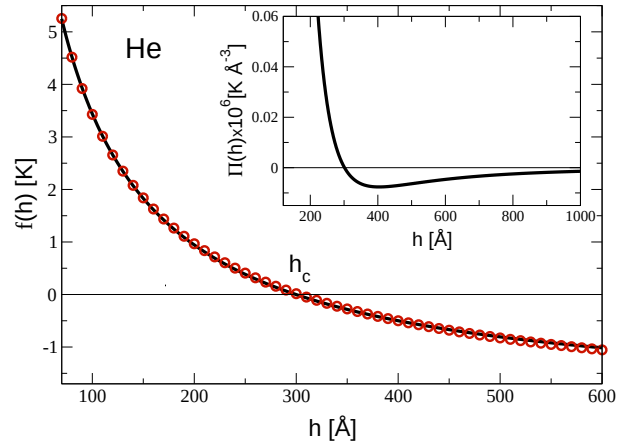


FIG. 10. Results for He, following the same procedure as in Fig. 9. With $\Pi(h) = f(h)/h^3$, the main panel shows the exact numerical evaluation of $f(h)$, solid line. The red circles represent a fit to the form $f(h) = -|\Pi_0| + \frac{\Pi_1}{h+L}$ (as in Eq. (1)), with $|\Pi_0| = 2.09$ K, $\Pi_1 = 676$ KÅ, $L = 22.1$ Å. These are the values used in the main text, Eq. (5). Inset: The full function $\Pi(h) = f(h)/h^3$. Notice the different scales on this graph compared to Fig. 9.

where the density $n_{\rm He} = 2.12 \times 10^{-2}$ Å$^{-3}$, the static polarizability $\alpha_{\rm He} = 1.38$ a.u., and the characteristic oscillator frequency $\omega_{\rm He} = 27.2$ eV. The atomic unit of polarizability is defined as 1 a.u. $= 0.148$ Å$^3$. For Nitrogen and Hydrogen, which have densities comparable to Helium but significantly larger polarizabilities, more accurate formulas based on the Clausius–Mossotti relation are typically used:

$$\varepsilon(i\omega) = 1 + \frac{4\pi n_A \alpha(i\omega)}{1 - \frac{4\pi}{3} n_A \alpha(i\omega)}, \quad A = {\rm N}_2, {\rm H}_2 \qquad \text{(A6)}$$

The dynamical polarizability $\alpha(i\omega)$ is defined as in Eq. (A5), i.e. has the form $\alpha(i\omega) = \frac{\alpha_{\rm A}}{1+(\omega/\omega_{\rm A})^2}$. For $H_2$ the parameters are: $n_{\rm H_2} = 2.04 \times 10^{-2}$ Å$^{-3}$, $\alpha_{\rm H_2} = 5.44$ a.u., $\omega_{\rm H_2} = 14.09$ eV. For $N_2$: $n_{\rm N_2} = 1.73 \times 10^{-2}$ Å$^{-3}$, $\alpha_{\rm N_2} = 11.74$ a.u., $\omega_{\rm N_2} = 19.32$ eV.

The VDW energy defined in Eq. (A1) has physical dimensions of energy per unit area. The disjoining pressure is defined as:

$$\Pi(h) = -\frac{\partial U_{\rm vdW}(h)}{\partial h}, \qquad \text{(A7)}$$

and describes the effective force per unit area between the two boundaries of the system (liquid–vapor and liquid–graphene). It is clear that the part of $\Pi(h)$ which comes from $\mathcal{U}_g(q, i\omega) > 0$ leads to positive pressure, i.e. favors film growth, while the part associated with $\mathcal{U}_d(q, i\omega) < 0$ is always negative, i.e. favors an instability. It is the competition between these two terms that leads to the spinodal de-wetting instability phenomenon.

Finally we return to the way we determine the all-important functional form of $\Pi(h)$, Eq. (1), which follows from the microscopic expressions Eqs. (A1),(A7). First we present the following qualitative considerations. As mentioned previously, it is useful to consider the contributions of the $\mathcal{U}_{d,g}(q, i\omega)$ terms separately. The (attractive) $\mathcal{U}_d$ part clearly leads to dependence of the form $\Pi(h) \sim -\frac{1}{h^3}$ which follows from counting powers of momenta in the integrals. The (repulsive) $\mathcal{U}_g$ part, however, exhibits a higher power due to the presence of graphene's polarization $\chi(q, i\omega)$. Since at intermediate frequencies, which are dominant in the integration, the dependence of $\chi(q, i\omega)$ on momentum is quadratic for low momenta, this leads to $\Pi(h) \sim \frac{1}{h^4}$ . The exact way this crossover happens has to be determined numerically, by evaluating the expression Eqs. (A1),(A7), which can be done with high accuracy. In Fig. 9 we show the way this procedure works for $N_2$ and, as another example, in Fig. 10 we present the results for He. Most importantly, we can conclude that the functional form of $\Pi(h)$, Eq. (1), used in the main text, is very accurate.

[1] J. N. Israelachvili, *Intermolecular and Surface Forces* (Academic Press, New York, 2011).

[2] P. G. De Gennes, Rev. Mod. Phys. **57**, 827 (1985).

[3] D. Bonn, J. Eggers, J. Indekeu, J. Meunier, and E. Rolley, Rev. Mod. Phys. **81**, 739 (2009).

[4] R. V. Craster and O. K. Matar, Rev. Mod. Phys. **81**, 1131 (2009).

[5] A. Oron, S. H. Davis, and S. G. Bankoff, Rev. Mod. Phys. **69**, 931 (1997).

[6] A. H. Castro Neto, F. Guinea, N. M. R. Peres, K. S. Novoselov, and A. K. Geim, Rev. Mod. Phys. **81**, 109 (2009).

[7] A. K. Geim and I. Grigorieva, Nature **499**, 419 (2013).

[8] K. S. Novoselov, A. Mishchenko, A. Carvalho, and A. H. Castro Neto, Science **353**, 461 (2016).

[9] A. Sharma, P. Harnish, A. Sylvester, V. N. Kotov, and A. H. Castro Neto, Phys. Rev. B **89**, 235425 (2014).

[10] N. S. Nichols, A. Del Maestro, C. Wexler, and V. N. Kotov, Phys. Rev. B **93**, 205412 (2016).

[11] B. Amorim, A. Cortijo, F. de Juan, A. G. Grushin, F. Guinea, A. Gutiérrez-Rubio, H. Ochoa, V. Parente, R. Roldán, P. San-Jose, J. Schiefele, M. Sturla, and M. A. H. Vozmediano, Phys. Rep. **617**, 1 (2016).

[12] V. N. Kotov, B. Uchoa, V. M. Pereira, F. Guinea, and A. H. Castro Neto, Rev. Mod. Phys. **84**, 1067 (2012).

[13] S. Sengupta, N. S. Nichols, A. Del Maestro, and V. N. Kotov, Phys. Rev. Lett. **120**, 236802 (2018).

[14] R. R. Nair, H. A. Wu, P. N. Jayaram, I. V. Grigorieva, and A. K. Geim, Science **335**, 442 (2012).

[15] J. S. Bunch, S. S. Verbridge, J. S. Alden, A. M. van der Zande, J. M. Parpia, H. G. Craighead, and P. L. McEuen, Nano Lett. **8**, 2458 (2008).

[16] A. Vrij, Discuss. Faraday Soc. **42**, 23 (1966).

[17] E. Ruckenstein and R. K. Jain, J. Chem. Soc. Faraday Trans. II **70**, 132 (1974).

[18] A. Sharma and R. Khanna, Phys. Rev. Lett. **81**, 3463 (1998).

[19] G. Reiter, A. Sharma, A. Casoli, M. O. David, R. Khanna, and P. Auroy, Langmuir **15**, 2551 (1999).

[20] V. S. Mitlin, J. Colloid Interface Sci. **156**, 491 (1993).

[21] R. Xie, A. Karim, J. F. Douglas, C. C. Han, and R. A. Weiss, Phys. Rev. Lett. **81**, 1251 (1998).

[22] A. Alizadeh Pahlavan, L. Cueto-Felgueroso, A. E. Hosoi, G. H. McKinley, and R. Juanes, J. Fluid Mech. **845**, 642 (2018).

[23] V. S. Mitlin and N. V. Petviashvili, Phys. Lett. A **192**, 323 (1994).

[24] D. Gentili, G. Foschi, F. Valle, M. Cavallini, and F. Biscarini, Chem. Soc. Rev. **41**, 4430 (2012).

[25] M. Rauscher, R. Blossey, A. Munch, and B. Wagner, Langmuir **24**, 12290 (2008).

[26] R. Seemann, S. Herminghaus, and K. Jacobs, Phys. Rev. Lett. **86**, 5534 (2001).

[27] R. Seemann, S. Herminghaus, and K. Jacobs, Journal of Physics: Condensed Matter **13**, 4925 (2001).

[28] R. Seemann, S. Herminghaus, C. Neto, S. Schlagowski, D. Podzimek, R. Konrad, H. Mantz, and K. Jacobs, Journal of Physics: Condensed Matter **17**, S267 (2005).

[29] J. W. Cahn, J. Chem. Phys. **42**, 93 (1965).

[30] I. E. Dzyaloshinskii, E. M. Lifshitz, and L. P. Pitaevskii, Adv. Phys. **10**, 165 (1961).

[31] E. M. Lifshitz and L. P. Pitaevskii, *Statistical Physics*, Part 2 (Pergamon Press, New York, 1980).

[32] V. Panella, R. Chiarello, and J. Krim, Phys. Rev. Lett. **76**, 3606 (1996).

[33] `http://www.nist.gov` (2020).

[34] M. S. Alnæs, J. Blechta, J. Hake, A. Johansson, B. Kehlet, A. Logg, C. Richardson, J. Ring, M. E. Rognes, and G. N. Wells, Arch. Num. Soft. **3**, 9 (2015).

[35] A. Logg, K.-A. Mardal, G. N. Wells, *et al.*, *Automated Solution of Differential Equations by the Finite Element Method* (Springer, 2012).

[36] A. Logg and G. N. Wells, ACM T. Math. Software **37**, 2 (2010).

[37] J. Crank and P. Nicolson, Math. Proc. Cambridge **43**, 50 (1947).

[38] C. R. Harris, K. J. Millman, S. J. van der Walt, R. Gommers, P. Virtanen, D. Cournapeau, E. Wieser, J. Taylor, S. Berg, N. J. Smith, R. Kern, M. Picus, S. Hoyer, M. H. van Kerkwijk, M. Brett, A. Haldane, J. Fernndez del Ro, M. Wiebe, P. Peterson, P. Grard-Marchant, K. Sheppard, T. Reddy, W. Weckesser, H. Abbasi, C. Gohlke, and T. E. Oliphant, Nature **585**, 357 (2020).

[39] P. Virtanen, R. Gommers, T. E. Oliphant, M. Haberland, T. Reddy, D. Cournapeau, E. Burovski, P. Peterson, W. Weckesser, J. Bright, S. J. van der Walt, M. Brett, J. Wilson, K. J. Millman, N. Mayorov, A. R. J. Nelson, E. Jones, R. Kern, E. Larson, C. J. Carey, İ. Polat, Y. Feng, E. W. Moore, J. VanderPlas, D. Laxalde, J. Perktold, R. Cimrman, I. Henriksen, E. A. Quintero, C. R. Harris, A. M. Archibald, A. H. Ribeiro, F. Pedregosa, P. van Mulbregt, and SciPy 1.0 Contributors, Nat. Methods **17**, 261 (2020).